

SUPERPIXEL GUIDED WEIGHTED LOW-RANK REPRESENTATION FOR NONLINEAR HYPERSPECTRAL UNMIXING

Touseef Ahmad^{a,b}, Anand S. Sahadevan^a, Soumyendu Raha^b, Rosly B. Lyngdoh^a, Deepak Putrevu^a

^aSpace Applications Centre, Ahmedabad, Indian Space Research Organization, India-380015,

^bDepartment of Computational and Data Sciences, Indian Institute of Science, Bangalore, India-560012

ABSTRACT

The Generalized Bilinear Mixing model (GBM) has gained significant prominence in the field of nonlinear hyperspectral image (HSI) unmixing, with recent advancements utilizing superpixel segmentation for the extraction of homogeneous patches. However, the application of the low-rank constraint (LRR) to each superpixel has been observed to disproportionately diminish smaller singular values, resulting in associated challenges. Building upon our prior investigation of the weighted LRR (WLRR) approach within the robust GBM model, which effectively mitigated bias by assigning appropriate weights to singular values, we extend this framework in the current study. Here, we employ entropy rate superpixel (ERS) segmentation to extract homogeneous patches, applying the weighted low-rank constraint and developing the robust GBM model (RGM-SG-WLRR) for nonlinear unmixing analysis. The proposed model is effectively solved using the Alternating Direction Method of Multipliers (ADMM) iterative scheme. Through extensive experimental analyses conducted on both simulated and real data cubes, our findings highlight the superior performance of the RGM-SG-WLRR model over alternative methods, as evidenced by its notable improvements in terms of root-mean-square error and signal-to-reconstruction error.

Index Terms— Hyperspectral unmixing; Generalized bi-linear model; Entropy rate super-pixel segmentation;

1. INTRODUCTION

The linear mixing model (LMM) [1, 2] is a fundamental approach that assumes each light ray interacting with an imaging sensor through the instantaneous field of view (IFOV) corresponds to the spectrum of a neighboring target. However, these simple assumptions fail to capture the complexities introduced by multiple interactions among light rays and neighboring targets, leading to non-linearity and reduced accuracy. Nonlinear mixing models (NLMs) [3] have emerged as an alternative solution to address these limitations.

Bilinear models, a subset of physics-inspired nonlinear models, consider interactions up to the second-order between light rays and materials in hyperspectral images (HSIs). While higher-order interactions are ignored due to their minimal impact on unmixing accuracy and the computational challenges they pose, bilinear models have garnered significant attention. Various bilinear models have been proposed, including Fan's model [4], Generalized Bilinear Mixing model (GBM) [5], Nascimento's model [6], and the polynomial-post nonlinear model [7].

Efforts to enhance GBM-based hyperspectral unmixing include introducing a Gradient Descent algorithm (GDA) for pixel-wise unmixing [8]. Semi-Non-negative Matrix Factorization (semi-NMF)

has also been employed for GBM-based HSI unmixing [9]. A Bound Projected Optimal Gradient Method (BPOGM) was proposed in [10] to achieve optimal convergence in GBM unmixing. To address non-Gaussian noise in HSIs, the bandwise GBM approach (NU-BGBM) was introduced [11]. More recently, robust GBM unmixing with super-pixel segmentation (RGBM-SS-LRR) [12] and weighted low-rank representation for GBM model [13] have been presented.

The RGBM-SS-LRR model utilizes entropy rate super-pixel (ERS) segmentation on the first principal component (PC) of the hyperspectral image. Each segment is processed using the RGBM-LRR algorithm, employing a low-rank constraint to capture spatial structure. However, the use of nuclear norm-based low-rank representation introduces bias due to its equal treatment of singular values.

This paper introduces the RGBM-SG-WLRR algorithm, which employs super-pixel guided weighted low-rank representation for robust GBM-based hyperspectral unmixing. The proposed method addresses challenges posed by nuclear norm and mixed noise in HSIs. ERS segmentation is applied to abundance matrices to capture homogeneous patches, and WLRR constraints are introduced on superpixels.

For WLRR, weighted nuclear norm minimization (WNNM) is employed, mitigating bias by assigning smaller weights to larger singular values. The remainder of the paper is structured as follows: Section 2 elaborates on the robust GBM approach with sparse and weighted low-rank representation, including ADMM strategy pseudocode. Section 3 presents experimental analyses on simulated and real datasets, while Section 4 concludes the paper.

2. SUPER-PIXEL GUIDED WEIGHTED LOW-RANK REPRESENTATION FOR GBM MODEL

A robust GBM (RGBM) model for hyperspectral imagery with L channels, M endmembers, and P samples can be represented as follows [11]:

$$\mathbf{Z} = \mathbf{A}\mathbf{X} + \mathbf{B}\mathbf{Y} + \mathbf{S} + \mathbf{N} \quad (1)$$

Here, $\mathbf{Z} \in \mathbb{R}^{L \times P}$ is the hyperspectral data matrix, \mathbf{A} is the end-member matrix, \mathbf{X} represents the abundance matrix, \mathbf{B} captures bilinear interactions, and \mathbf{Y} holds corresponding bilinear coefficients. \mathbf{S} & $\mathbf{N} \in \mathbb{R}^{L \times P}$ denote sparse and dense noise, respectively [11].

To capture spatially correlated pixels, the hyperspectral image (HSI) is segmented into homogeneous regions that follow the low-rank property. We adopt the entropy rate super-pixel (ERS) segmentation approach, which is computationally efficient [14] and tends to yield homogeneous clusters of similar sizes. ERS segmentation is applied iteratively on the abundance data cube of HSI within the proposed RGBM-SG-WLRR algorithm, capturing the low-rank property of spectrally similar neighborhood pixels [13].

Consequently, the super-pixel-based weighted low-rank for the robust GBM model can be formulated as follows:

$$\min_{\mathbf{X}, \mathbf{Y}, \mathbf{S}} \frac{1}{2} \|\mathbf{Z} - (\mathbf{A}\mathbf{X} + \mathbf{B}\mathbf{Y} + \mathbf{S})\|_F^2 + \alpha \|\mathbf{S}\|_1 + \lambda \sum_{i=1}^p \|\mathbf{X}^{(i)}\|_{b,*}$$

subject to $\mathbf{X} \geq \mathbf{0}$ and $\mathbf{0} \leq \mathbf{Y} \leq \mathbf{Y}^*$ (2)

Here, p is the number of superpixels, $\mathbf{X}^{(i)}$ is the fractional abundance matrix of the i^{th} superpixel, and $\|\cdot\|_{b,*}$ is the weighted nuclear norm. The weighted nuclear norm accounts for the singular values $\sigma_l(\mathbf{X}^{(i)})$ with weights b_l to efficiently estimate the rank [13]. Additional low-rank regularization is included to improve the algorithm's performance due to correlated pixels within each segment.

The pseudo-code of the aforementioned iterative scheme is outlined in Algorithm 1. For a more comprehensive understanding of the auxiliary variables in the pseudo-code, as well as for stability and convergence analysis of the iterative scheme, please follow the reference [13].

Algorithm 1: Pseudo-code:RGBM-SG-WLRR

Input: $\mathbf{Z}, \mathbf{A}, \mathbf{B}, \mu$
Output: $\mathbf{X}, \mathbf{Y}, \mathbf{S}$

- 1 **Initialization:** $\mathbf{X}, \mathbf{Y}, \mathbf{U}_1, \mathbf{U}_2, \mathbf{U}_3, \Lambda_1, \Lambda_2, \Lambda_3$, for $k=0$
- 2 **While not converged Do**
- 3 **for** $i=1$ to p
- 4 $\mathbf{U}_1^{(i)k+1} = \text{SVT}_{b, \frac{\lambda}{\mu}}(\mathbf{X}^{(i)k} + \Lambda_1^{(i)k})$;
- 5 **end for**
- 6 $\mathbf{X}^{k+1} = [\mathbf{A}^T \mathbf{A} + 2\mu \mathbf{I}]^{-1} [\mathbf{A}^T (\mathbf{Z} - \mathbf{B}\mathbf{Y}^k - \mathbf{S}^k) + \mu(\mathbf{U}_1^k - \Lambda_1^k + \mathbf{U}_2^k - \Lambda_2^k)]$;
- 7 $\mathbf{U}_2^{k+1} = \max(\mathbf{X}^{k+1} + \Lambda_2^k, \mathbf{0})$;
- 8 $\mathbf{Y}^{k+1} = [\mathbf{B}^T \mathbf{B} + \mu \mathbf{I}]^{-1} [\mathbf{B}^T (\mathbf{Z} - \mathbf{A}\mathbf{X}^{k+1} - \mathbf{S}^k) + \mu(\mathbf{U}_3^k - \Lambda_3^k)]$;
- 9 $\mathbf{U}_3^{k+1} = \min(\max(\mathbf{Y}^{k+1} + \Lambda_3^k, \mathbf{0}), \mathbf{Y}^*)$;
- 10 $\mathbf{S}^{k+1} = \mathcal{S}_\alpha(\mathbf{Z} - \mathbf{A}\mathbf{X}^{k+1} - \mathbf{B}\mathbf{Y}^{k+1})$;
- 11 $\Lambda_1^{k+1} = \Lambda_1^k - (\mathbf{U}_1^{k+1} - \mathbf{X}^{k+1})$
- 12 $\Lambda_2^{k+1} = \Lambda_2^k - (\mathbf{U}_2^{k+1} - \mathbf{X}^{k+1})$
- 13 $\Lambda_3^{k+1} = \Lambda_3^k - (\mathbf{U}_3^{k+1} - \mathbf{Y}^{k+1})$
- 14 **Update k:** $k=k+1$
- 15 **end while :** Some stopping criteria[15].
- 16 **Return:** $\mathbf{X} = \mathbf{X}^{k+1}, \mathbf{Y} = \mathbf{Y}^{k+1}, \mathbf{S} = \mathbf{S}^{k+1}$.

3. RESULTS AND DISCUSSION

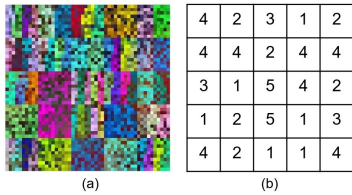


Fig. 1. (a)Experiment-1:FCC image of simulated data with SNR=30dB , (b) Table for the rank of each block.

Table 1. Accuracy assessment in Exp.-1 with varying SNR.

SNR	Index	FCLS	NU-BGBM	RGBM-SS-LRR	RGBM-SG-WLRR
20 dB	SRE(dB)	-1.0302	16.3064	16.7825	19.2243
	aRMSE	0.2045	0.0278	0.0263	0.0199
	sRMSE	0.1117	0.0615	0.0616	0.0617
	Time(s)	3.8109	75.6754	42.0276	34.6266
	Parameters	-	$\alpha = 10^{-1}$	$\lambda = 10^{-3}, \alpha = 10^{-3}$	$\lambda = 10^{-3}, \alpha = 10^{-3}$
		-			
30 dB	SRE(dB)	-0.6469	23.2692	24.2726	27.5642
	aRMSE	0.1988	0.0127	0.0113	0.0077
	sRMSE	0.0953	0.0505	0.0504	0.0504
	Time(s)	2.6433	82.7976	41.51	34.7633
	Parameters	-	$\alpha = 10^{-1}$	$\lambda = 10^{-3}, \alpha = 10^{-2}$	$\lambda = 10^{-3}, \alpha = 10^{-2}$
		-			
40 dB	SRE(dB)	-0.7473	30.1948	29.9562	32.7447
	aRMSE	0.2036	0.0058	0.0059	0.0043
	sRMSE	0.1150	0.0494	0.0494	0.0494
	Time(s)	2.6659	82.8183	42.8996	37.5871
	Parameters	-	$\alpha = 10^{-2}$	$\lambda = 10^{-3}, \alpha = 10^{-2}$	$\lambda = 10^{-3}, \alpha = 10^{-2}$
		-			
50 dB	SRE(dB)	-0.8217	34.5778	31.0686	34.7605
	aRMSE	0.1987	0.0034	0.0051	0.0033
	sRMSE	0.0950	0.502	0.501	0.0501
	Time(s)	4.949	76.2081	33.3362	33.2747
	Parameters	-	$\alpha = 10^{-3}$	$\lambda = 10^{-3}, \alpha = 10^{-2}$	$\lambda = 10^{-4}, \alpha = 10^{-2}$
		-			

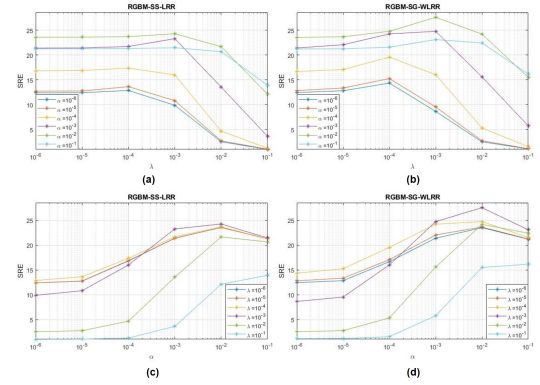


Fig. 2. Comparison of SRE estimated over simulated dataset with SNR=30dB using RGBM-SS-LRR(1st Column) and RGBM-SG-WLRR(2nd Column) against varying λ and α .

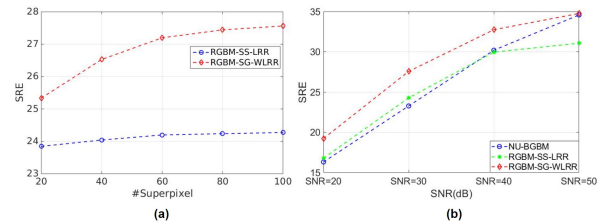


Fig. 3. (a) Comparison of estimated SRE by RGBM-SS-LRR and RGBM-SG-WLRR against varying number of superpixel in Exp-1 ($SNR = 30dB$), (b) comparison of estimated SRE by NU-BGBM, RGBM-SS-LRR and RGBM-SG-WLRR against varying SNR of simulated data in Exp-1.

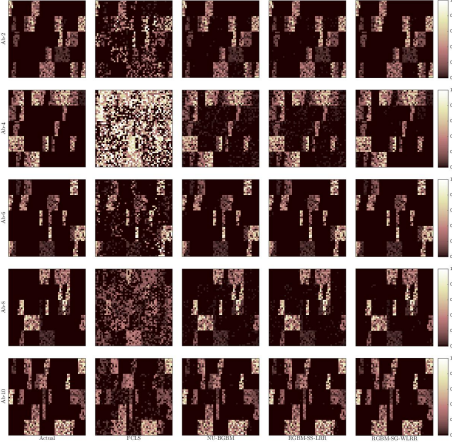


Fig. 4. Comparison of actual abundance maps of even number of endmembers (Experiment-1 with $SNR=30dB$) with estimated abundance maps using FCLS (2nd Column), NU-BGBM(3rd Column), RGBM-SS-LRR (4th Column) and RGBM-SG-WLRR(5th Column).

3.1. Experiment-1: Simulated Dataset

Simulated HSI with varying SNR were generated (as mentioned in [12] for evaluating the performance of the proposed RGBM-SG-WLRR algorithm. The simulated HSI was organized into 5×5 blocks, and each block contains 100 pixels i.e. block-size 10×10 . To construct the simulated HSI, ten endmembers were chosen at random from the USGS spectral library (<https://www.usgs.gov/labs/spec-lab>), and the rank (of abundance matrix) in each block was generated at random from rank=1 to rank=5, as shown in Fig.1(b). To add mixed noise to the HSI, three types of noises were generated: Gaussian noise using zero-mean i.i.d, impulse noise, and deadlines (strips). Band no. 20 – 30 and band no. 80 – 90 were contaminated with 10% impulse noise and deadlines respectively. For bi-linear abundance matrix generation, the non-linearity coefficients were drawn uniformly in the range of $[0, 1]$. FCC of simulated dataset with $SNR = 30dB$ is displayed in Fig. 1(a).

Studies [11, 12] have already shown that RGBM-SS-LRR and NU-BGBM algorithms perform significantly better than the fully constrained least square method (FCLS), GDA, semi-NMF, and BPOGM. We consider FCLS, NU-BGBM, and RGBM-SS-LRR to discuss the performance of RGBM-SG-WLRR. The parameters $\mu = 10^{-2}$, $tolerance = 10^{-6}$, and $iteration = 1000$ were fixed in this experiment for a fair comparison with other recent algorithms [12]. $\lambda, \alpha \in \{0, 10^{-6}, 10^{-5}, 10^{-4}, 10^{-3}, 10^{-2}, 10^{-1}\}$ were chosen for the fair comparison (given in [12] of the results). Extensive analysis was carried out over the simulated data with varying SNR from $20dB$ to $50dB$. Optimum parameters corresponding to higher SRE have been identified, and the results were tabulated in Table 1.

FCLS did not perform well in all cases of SNR. RGBM-SS-LRR showed higher SRE (in $SNR = 20dB$ and $SNR = 30dB$), lower aRMSE, and less computational time than the NU-BGBM algorithm. In the case of $SNR = 40dB$ and $SNR = 50dB$, NU-BGBM was able to achieve higher SRE and lower aRMSE than RGBM-SS-LRR. From Table 1, we can see that the proposed method (RGBM-SG-WLRR) is significantly superior to both NU-

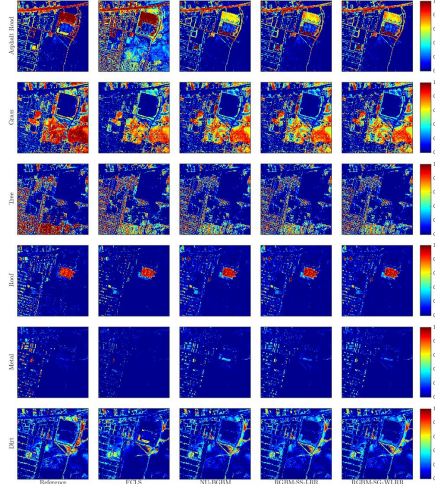


Fig. 5. Comparison of reference abundance maps (1st column) with estimated abundance maps using FCLS (2nd column), NU-BGBM (3rd column), RGBM-SS-LRR(4th column) and RGBM-SG-WLRR(5th column) respectively.

BGBM and RGBM-SS-LRR algorithms in all cases. Abundance maps of selected endmembers corresponding to $SNR = 30dB$ are displayed in Fig. 4. Results obtained from RGBM-SS-LRR and RGBM-SG-WLRR were dependent on the sparsity (α) and low-rank (λ) parameters. Thus, SRE for fixed α and varying λ corresponds to RGBM-SS-LRR and RGBM-SG-WLRR were compared and plotted in Fig. 2(a) and Fig. 2(b), respectively. Fig. 2 shows that SRE increases to a certain limit, after which it starts decreasing for all cases of α with varying λ for both algorithms. Similarly, SRE for fixed λ and varying α correspond to RGBM-SS-LRR and RGBM-SG-WLRR were plotted in Fig. 2(c) and Fig. 2(d), respectively. This figure shows that SRE increases to a certain limit, after which it starts decreasing for all λ with varying α for RGBM-SS-LRR and RGBM-SG-WLRR. From both figures, it is observed that the proposed algorithm achieved higher SRE than RGBM-SS-LRR for all cases. From Fig. 3(a) (Exp.-1 with $SNR=30dB$), it is observed that the number of super-pixel segments increases SRE also increases and saturates. However, the proposed method was able to achieve higher SRE as compared to RGBM-SS-LRR irrespective of the number of super-pixels.

Figure 3(b) shows SREs of the NU-BGBM, RGBM-SS-LRR, and RGBM-SG-WLRR as a function of SNR (see Fig. 3(b)). The SREs of all three algorithms increase with the increase in SNR, which may be attributed to the fact that all these algorithms consider the sparsity property of the sparse noise while unmixing. Mei et al. [12] observed that the SREs of the FCLS, GDA, Semi-NMF, BPOGM show no improvements for different SNRs since these methods do not consider sparse noise while unmixing. From Fig. 3(b), it can be observed that the proposed method achieved higher SRE than NU-BGBM and RGBM-SS-LRR on HSI with lower SNR.

3.2. Experiment-2: Real Dataset (Urban)

Experiment-2 was performed using the real dataset (Urban dataset which is accumulated by the Hyperspectral Digital Imagery Col-

lection Experiment (HYDICE) (<http://www.escience.cn/people/feiyunZHU/DatasetGT.html>) [16]. In this experiment, endmembers were estimated using Vertex Component Analysis (VCA) [17]. FCLS, NU-BGBM, RGBM-SS-LRR, and RGBM-SG-WLRR were compared in this experiment (see Fig. 5). Results were compared with the reference abundance maps (First column in Fig. 5) [16]. As reported in [11], the fractional abundance maps of Metal and Dirt measured by different approaches were consistent. As shown in Fig. 5, the fractional abundance maps obtained from NU-BGBM, RGBM-SS-LRR, and RGBM-SG-WLRR algorithms were very consistent. The abundance map of metal obtained from NU-BGBM was over-estimated as compared to RGBM-SS-LRR and RGBM-SG-WLRR. Due to the non-availability of actual abundance maps in real data experiments, estimation of SRE and aRMSE were not possible, and sRMSE cannot be considered as a robust measure to perform the accuracy assessment.

However, the solutions obtained from both algorithms (RGBM-SS-LRR and RGBM-SG-WLRR) depend on two parameters such as sparsity α and low-rank λ . Reconstruction error (sRMSE) was estimated for both the algorithms against varying α and λ , which follows a similar pattern as mentioned in Fig. 2.

4. CONCLUSION

In this paper, the RGBM-SG-WLRR algorithm based on superpixel-guided weighted LRR was introduced for nonlinear unmixing of HSIs. ERS segmentation was employed on the abundance map for generating superpixels, and each superpixel follows the low-rank property. A weighted nuclear norm minimization was performed on each superpixel, and this constraint is combined with the main objective function of the unmixing problem. By assigning higher weights to smaller values and smaller weights to larger values, the WLRR eliminates the penalty bias between larger and smaller singular values. A sparsity constraint was also applied over sparse noise terms to suppress the effect of noise during the unmixing process. Two experiments were performed to assess the performance of the proposed algorithm relative to other existing methods. Results obtained from weighted LRR were significantly better than LRR. High SRE, low aRMSE, and low sRMSE of the super-pixel guided WLRR approach confirm the effectiveness of the presented algorithm over existing methods.

5. REFERENCES

- [1] Jiaojiao Wei and Xiaofei Wang, "An overview on linear unmixing of hyperspectral data," *Mathematical Problems in Engineering*, vol. 2020, 2020.
- [2] José M Bioucas-Dias, Antonio Plaza, Nicolas Dobigeon, Mario Parente, Qian Du, Paul Gader, and Jocelyn Chanussot, "Hyperspectral unmixing overview: Geometrical, statistical, and sparse regression-based approaches," *IEEE journal of selected topics in applied earth observations and remote sensing*, vol. 5, no. 2, pp. 354–379, 2012.
- [3] Rob Heylen, Mario Parente, and Paul Gader, "A review of nonlinear hyperspectral unmixing methods," *IEEE Journal of Selected Topics in Applied Earth Observations and Remote Sensing*, vol. 7, no. 6, pp. 1844–1868, 2014.
- [4] Wenyi Fan, Baixin Hu, John Miller, and Mingze Li, "Comparative study between a new nonlinear model and common linear model for analysing laboratory simulated-forest hyperspectral data," *International Journal of Remote Sensing*, vol. 30, no. 11, pp. 2951–2962, 2009.
- [5] Abderrahim Halimi, Yoann Altmann, Nicolas Dobigeon, and Jean-Yves Tournet, "Nonlinear unmixing of hyperspectral images using a generalized bilinear model," *IEEE Transactions on Geoscience and Remote Sensing*, vol. 49, no. 11, pp. 4153–4162, 2011.
- [6] José MP Nascimento and José M Bioucas-Dias, "Nonlinear mixture model for hyperspectral unmixing," in *Image and Signal Processing for Remote Sensing XV*. International Society for Optics and Photonics, 2009, vol. 7477, p. 74770I.
- [7] Rob Heylen, Paul Scheunders, Anand Rangarajan, and Paul Gader, "Nonlinear unmixing by using different metrics in a linear unmixing chain," *IEEE Journal of Selected Topics in Applied Earth Observations and Remote Sensing*, vol. 8, no. 6, pp. 2655–2664, 2014.
- [8] Abderrahim Halimi, Yoann Altmann, Nicolas Dobigeon, and Jean-Yves Tournet, "Unmixing hyperspectral images using the generalized bilinear model," in *2011 IEEE International Geoscience and Remote Sensing Symposium*. IEEE, 2011, pp. 1886–1889.
- [9] Naoto Yokoya, Jocelyn Chanussot, and Akira Iwasaki, "Nonlinear unmixing of hyperspectral data using semi-nonnegative matrix factorization," *IEEE Transactions on Geoscience and Remote Sensing*, vol. 52, no. 2, pp. 1430–1437, 2013.
- [10] Chang Li, Yong Ma, Jun Huang, Xiaoguang Mei, Chengyin Liu, and Jiayi Ma, "Gbm-based unmixing of hyperspectral data using bound projected optimal gradient method," *IEEE Geoscience and Remote Sensing Letters*, vol. 13, no. 7, pp. 952–956, 2016.
- [11] Chang Li, Yu Liu, Juan Cheng, Rencheng Song, Hu Peng, Qiang Chen, and Xun Chen, "Hyperspectral unmixing with bandwise generalized bilinear model," *Remote Sensing*, vol. 10, no. 10, pp. 1600, 2018.
- [12] Xiaoguang Mei, Yong Ma, Chang Li, Fan Fan, Jun Huang, and Jiayi Ma, "Robust gbm hyperspectral image unmixing with superpixel segmentation based low rank and sparse representation," *Neurocomputing*, vol. 275, pp. 2783–2797, 2018.
- [13] Touseef Ahmad, Soumyendu Raha, Rosly B Lyngdoh, Anand S Sahadevan, Praveen K Gupta, and Arundhati Misra, "Robust generalized bilinear model with weighted low-rank representation for hyperspectral image unmixing," *Journal of Applied Remote Sensing*, vol. 16, no. 2, pp. 024524–024524, 2022.
- [14] Ming-Yu Liu, Oncel Tuzel, Srikumar Ramalingam, and Rama Chellappa, "Entropy rate superpixel segmentation," in *CVPR 2011*. IEEE, 2011, pp. 2097–2104.
- [15] Touseef Ahmad, Rosly Boy Lyngdoh, Anand S Sahadevan, Soumyendu Raha, Praveen K Gupta, and Arundhati Misra, "Four-directional spatial regularization for sparse hyperspectral unmixing," *Journal of Applied Remote Sensing*, vol. 14, no. 4, pp. 046511, 2020.
- [16] Feiyun Zhu, "Hyperspectral unmixing: ground truth labeling, datasets, benchmark performances and survey," *arXiv preprint arXiv:1708.05125*, 2017.
- [17] José MP Nascimento and José MB Dias, "Vertex component analysis: A fast algorithm to unmix hyperspectral data," *IEEE transactions on Geoscience and Remote Sensing*, vol. 43, no. 4, pp. 898–910, 2005.